NanoCommunication-based Flow Path Mapping for NanoSensors in Underground Oil Reservoirs

Liuyi Jin, Zhipei Yan, Lihua Zuo**, Radu Stoleru
Texas A&M University, College Station, TX, USA
**Texas A&M University-Kingsville, Kingsville, TX, USA
{liuyi,yanzp,stoleru}@tamu.edu,lihua.zuo@tamuk.edu

ABSTRACT

Oil reservoir exploration is booming, given the increasing energy demand worldwide. The existence of Impermeable Regions (IR) in the oil reservoir (i.e., underground areas that allow only few hydrocarbons-collecting fluids to pass through) still hinders current production performance to a great extent. Research efforts have been invested into IR detection and mapping. The state of the art solution [1] leverages nanoscale sensor networks to approximately characterize the location of a single IR in the underground oil reservoir. However, the characterization accuracy is rather low. In addition, existing solutions are not applicable to more heterogeneous reservoirs, which reflects, in fact, a more realistic problem scenario. In this paper, we investigate and address the limitations of state of the art solutions in two aspects: 1) we provide a sub-terahertz (THz) communication channel to reflect realism of nanocommunication in the underground; 2) we develop a sensor path (i.e., simulated streamlines along which sensors are assumed to flow) reconstruction workflow to map a more heterogeneous reservoir with more IRs. Through simulations, we show that our proposed solution achieves an improvement of IRs mapping performance, when compared to the state of the art solution.

CCS CONCEPTS

• **Applied computing** → **Telecommunications**; • **Computing methodologies** → **Shape modeling**.

KEYWORDS

Nanonetworks, Simulation, 2D Geometry Reconstruction

ACM Reference Format:
Liuyi Jin, Zhipei Yan, Lihua Zuo**, Radu Stoleru. 2020. NanoCommunication-based Flow Path Mapping for NanoSensors in Underground Oil Reservoirs. In *The Seventh Annual ACM International Conference on Nanoscale Computing and Communication (NANOCOM '20), September 23–25, 2020, Virtual Event, USA.* ACM, New York, NY, USA, 7 pages. https://doi.org/10.1145/3411295.3411309

NANOCOM '20, September 23–25, 2020, Virtual Event, USA

ACM ISBN 978-1-4503-8083-6/20/09…$15.00
https://doi.org/10.1145/3411295.3411309

1 INTRODUCTION

The demand for energy is continually increasing. As indicated [2], the energy requirements are expected to increase 1.5 times in the next two decades. In supplying the energy worldwide, the oil and gas industry still plays an important role [3]. Energy companies are always seeking efficient ways to extract resources from Underground Reservoirs (UR), e.g., oil, gas or geothermal reservoirs. To achieve efficient extraction, they perform *reservoir characterization* before production. Reservoir characterization is a commonly used technique in the field to facilitate the understandings of the UR. Specifically, the vertical and lateral heterogeneity in the reservoir can be inferred through analysis of various datasets [4]. The dataset typically consists of data of miscellaneous sources in the field. By appropriately leveraging petroleum engineering techniques to solve posed inverse problems given the dataset, geological and fluid properties of interests (such as lithology, porosity and fluid saturations) can be obtained. For instance, in [5], wireline dipole and monopole data is utilized to perform high resolution imaging of far-field horizontal and slanted well structures. However, due to the high costs of collecting data from field, most of these methods are not economical. In addition, the inherent noise in the field data usually leads to inaccurate reservoir characterization results.

Impermeable area detection and characterization are key parts of characterization for conventional reservoir exploration. However, only few efforts have been dedicated to this problem. Traditional methods, such as well testing, have been used to map the spatial information of impermeable areas [6, 7]. To detect an impermeable area, well testing used to be the only available technique, which generates an imprecise picture of the underground IR geometry. More recently, [8] points out seismic signals can be reflected by reservoirs and seals, which are two important components of stratigraphic traps. The reflected signals vary in configuration, amplitude, continuity, frequency and interval velocity. Hence, the variational reflected signals can be leveraged to infer stratification and depositional features. In unconventional reservoirs, the reservoirs themselves can be regarded as an IR. Researchers [9, 10], from a fracture simulation point of view, have worked on fracture geometry characterization and monitoring. However, none of these efforts provides accurate characterization of IR location and shape.

In [1], a new solution was proposed for the IR mapping problem in conventional oil reservoirs. The solution is based on 2D-reconstruction computer graphics techniques. Nanoscale sensors equipped with terahertz (THz) communication capabilities were employed. The nanosensors are assumed to flow on *streamlines* along with hydrocarbon fluids. In this paper, we employ similar techniques (e.g., nanocommunication and streamline simulation),

but we investigate the problem of more complex IR layouts. The main contributions of this paper are summarized as follows:

- It presents a (sub-)Thz communication channel model to approximate the communication behavior of nanosensors when they flow through an underground reservoir.
- It presents a nanosensor path reconstruction problem formulated as a streamline reconstruction workflow.
- It presents a solution to the path reconstruction problem for underground environments with higher heterogeneity, than state of the art solutions [1], thus addressing more realistic and complex underground scenarios.

This paper is structured as follows: Section 2 reviews background material and state of the art solutions for reservoir mapping. Section 3 gives the system model and formulates the research problem. In Sections 4 and 5, we present the proposed solution and implementation, and performance evaluation results, respectively. Finally, we conclude the paper in Section 6 with ideas for future work.

2 STATE OF THE ART

In [1], for the first time the IR mapping problem is solved using nanodevices equipped with wireless communication capabilities. The initial results seemed promising in that the proposed algorithm can minimize the number of wells while finding the location of a single impermeable area. However, the final characterization still deviates much from expectations. For instance, the first evaluation metric $\alpha(k)$ indicates 40% error, indicating a large potential of improvement. Besides, the algorithm in [1] is feasible only for the problem with one IR, and not applicable to oil production environments with higher heterogeneity (e.g., more than one IR), which are more realistic in the real world. In addition, the THz channel model is simplistic and the feasibility of the THz-based communication for oil exploration is not investigated.

A few researchers addressed the communication channel modelling problem in nanoscale and underground environments [11, 12]. [13] points out applying optical nano-antenna arrays and beamforming could help increase the EM transmission distance to a few millimeters. [14] is pioneering work on THz channel modelling for underground oil reservoirs by referencing developed channel models. In the numerical results, when the transmitting power and minimum received signal power is set to be 0 dBm and -100 dBm respectively, the communication range of the THz EM waves in oil and water mixture is no more than 1 cm in the 0.1 Thz to 120.0 THz band. [15] further employs the developed models to model the communication channels in oil for megahertz (MHz) and gigahertz (GHz) frequencies. Nevertheless, the hyper-parameters of neither [14] nor [15] are clearly investigated, to address the feasibility of THz-based nanocommunication for oil exploration.

A streamline simulation using numerical simulations was developed for petroleum production environments [16, 17]. It aims to provide references and better understanding of production system performance in four aspects: reservoir-flow surveillance, flow simulation, history matching and flood management [18]. Recently, although various applications in petroleum engineering solve optimization and reconstruction problems through streamline simulation techniques [18], employing streamline simulation techniques for mapping IRs is still an open research area.

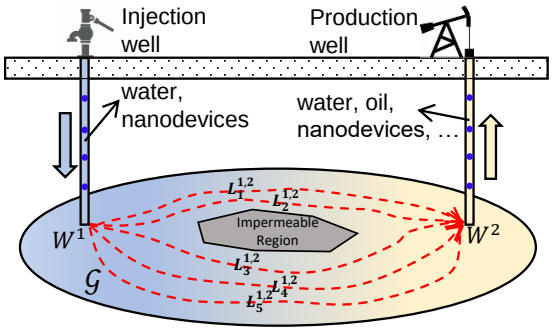

Figure 1: Single Impermeable Region (IR) mapping in oil exploration using one pair of wells, (W^1,W^2). Nanodevices (blue circles) inserted at W^1 flow along the k-th streamline path $L_k^{1,2}$ until they are collected at W^2.

3 PRELIMINARIES AND PROBLEM FORMULATION

Before we formulate the problem of impermeable region mapping for oil reservoirs, we present the behavior of a nanodevice in the system through a mobility model, a channel model and a communication model. As shown in Figure 1, nanodevices, equipped with wireless communication (sub-)THz radios [14], are injected into the reservoir through injection wells. It's important to note we continuously deploy massive nanosensors into the reservoir continuously in practice. This is due to the fact that real reservoirs are usually in kilometers scale, while the nanosensors are in nanoscale. Each nanodevice is a receiver and transmitter and flows along a streamline. Therefore, in this paper, the streamlines are modelled as flow paths of those nanodevices. Nanodevices transmit beacons periodically and record the received signal strength indicator (RSSI) values from other nanodevices. When nanodevices are retrieved from production wells, the RSSI data stored in each receiver is used for interpreting the distances between transmitters and receivers, which will be further leveraged to map the underground impermeable regions. In this paper, we assume the deployed nanodevices can only communicate with other nanodevices flowing along the same streamline.

We introduce two definitions of physical variables from petroleum engineering for better understanding of our problem formulation: *porosity* ρ is defined as the volume of pores within one unit of soil/rock, *water saturation* w_{sat} is the volume of water contained in each unit volume of pores in soil/rock:

$$\rho = \frac{V_{pore}}{V} \qquad w_{sat} = \frac{V_{water}}{V_{pore}} \tag{1}$$

3.1 System Models

We consider a 2D oil reservoir plane $\mathcal{G}$ to be explored for oil as shown in Figure 1. The exploration is performed by the wells $\{W^i | i \in I\}$, where I is the index set of all wells. Each well W^i can be either an injection well or production well. Water and nanodevices are injected into injection wells. As nanodevices flow along

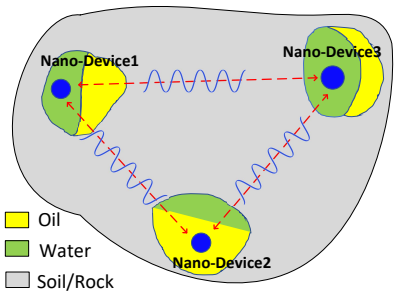

Figure 2: Cross-area plot: nanoSensors are flowing in the underground pores while communicating with each other using THz radios.

streamlines through the underground, they actually flow through microscale or even nanoscale pores as shown in Figure 2. Those pores are filled with water, oil or both. Oil, water and nanodevices are collected from production wells where the distance between transmitters and receivers is retrieved. It should be noted that wells that are initially injection wells can become production wells later, and vice versa.

3.1.1 Mobility Model. Mobility model defines how nanosensors move in the underground. Between a well pair $(W^i, W^j), i \neq j$, where W^i used as the injection and W^j used as the production, We collect all streamlines as $\{L_k^{i,j} | k \in K^{i,j}\}$. We deploy nanodevices at a fixed rate, assuming there are always $N_k^{i,j}$ nanodevices along the chosen streamline $L_k^{i,j}$ shown in Figure 3. Streamlines are modelled as the flow path of nanodevices. We assume that each nanodevice will strictly follow one streamline in the underground reservoir.

3.1.2 Channel Model. In this subsection we discuss how we model the communication channel between nanosensors. Figure 2 is the cross-area plot showing how nanodevices move through the underground reservoir pores in nano(micro-)scale. The grey area outlined the matrix materials inside rocks. The pores are remained open for water, oil and nanodevice mixtures to flow through. In this paper, we assume no gas in pores in the underground. Nanodevices are capable of (sub-)THz radio communication with other nanodevices while flowing through pores.

We consider nanocommunication in real oil production. The total propagation path loss, PL, consists of 3 parts: spread loss PL^s, propagation loss through oil PL^{oil}, and soil PL^{soil}. PL^{oil} and PL^{soil} are weighted by leveraging definitions in Equation (1). It should be noted that the absorption loss through water is already considered in the absorption loss through soil. PL is given in Equation (2), and PL^s is given in Equation (3).

$$PL = PL^s + \rho\,(1 - w_{sat})\,PL^{oil} + (1 - \rho\,(1 - w_{sat}))PL^{soil} \tag{2}$$

$$PL^s = 20\lg\left(\frac{4\pi f d}{c}\right) \tag{3}$$

where f is frequency in Hz, d is the propagation distance in $meter$, c is the light speed in m/s. In [11, 15], the EM wave propagation loss through oil and soil has the same expression shown in Equation (4).

$$PL^{oil(soil)} = 6.4 + 20\lg(d) + 20\lg(\beta) + 8.69\alpha d \tag{4}$$

where α (dB/m), attenuation constant, and β (rad/m), phase constant, can be derived as in Equation (5) [19].

$$\begin{aligned}\alpha &= 2\pi f\sqrt{\frac{\mu\epsilon'_{cr}\epsilon_0}{2}\left[\sqrt{1+\left(\frac{\epsilon''_{cr}}{\epsilon'_{cr}}\right)^2}-1\right]}\\ \beta &= 2\pi f\sqrt{\frac{\mu\epsilon'_{cr}\epsilon_0}{2}\left[\sqrt{1+\left(\frac{\epsilon''_{cr}}{\epsilon'_{cr}}\right)^2}+1\right]}\end{aligned} \tag{5}$$

where f is the frequency in Hz, μ is the magnetic permeability set to be $1.26 \times 10^{-6} H/m$, ϵ_0 is the permittivity in free space, i.e. $8.854\times10^{-12} F/m$. ϵ'_{cr} and ϵ''_{cr} are real and imaginary part of *complex relative permittivity* or *complex dielectric constant* ϵ_{cr}, respectively. It should be noted that ϵ'_{cr} and ϵ''_{cr} are dimensionless variables depending on propagation medium properties. For **oil** medium, we adopted the parameter setup in [15] at 2.45 GHz, i.e., $\epsilon'_{cr} = 2.19$ and $\epsilon''_{cr} = -0.007$. For **soil** medium, we obtain ϵ'_{cr} and ϵ''_{cr} by following the model in [20, 21] as shown in Equations (6)-(11). The corresponding hyper-parameters are shown in Table 1 where the variables with unit 1 are dimensionless variables.

$$\epsilon_{cr} = \epsilon'_{cr} - j\epsilon''_{cr} \tag{6}$$

$$\epsilon'_{cr} = \left[1 + \frac{\rho_b}{\rho_s}\left((\epsilon_s)^{\alpha'}\right) + (m_v)^{\beta'}\left(\epsilon'_{fw}\right)^{\alpha'} - m_v\right]^{1/\alpha'} \tag{7}$$

$$\epsilon_s = (1.01 + 0.44\rho_s)^2 - 0.062 \tag{8}$$

$$\epsilon''_{cr} = \left[(m_v)^{\beta''}\left(\epsilon''_{fw}\right)^{\alpha'}\right]^{1/\alpha'} \tag{9}$$

$$\beta' = 1.2748 - 0.519S - 0.152C \tag{10}$$

$$\beta'' = 1.33797 - 0.603S - 0.166C \tag{11}$$

Table 1: Parameters for calculating the complex dielectric constant ϵ_{cr}

Parameter	Physical Mean	Value	Unit
ρ_b	bulk density	1.5	g/m^3
ρ_s	specific density of solid soil particles	2.66	g/m^3
ϵ_s	dielectric constant of soil solids		1
α'	empirically determined	0.65	
β'	empirically determined		
β''	empirically determined		
ϵ'_{fw}	real part of complex dielectric constant of water	4.77 [22]	1
ϵ''_{fw}	imaginary part of complex dielectric constant of water	3.78 [22]	1
S	sand particle percent	0.5	1
C	clay particle percent	0.15	1
m_v	water volume fraction	0.05	1

The total path loss PL is computed using Equation (2). The water saturation w_{sat} and porosity ρ are set to be 0.25 and 0.2, respectively. The path loss with respect to frequency and distance is shown in Figure 4. From Figure 4, we know that path loss PL in Equation (2) is a function of frequency f and distance d, and can be defined as:

$$PL = PL(d, f). \tag{12}$$

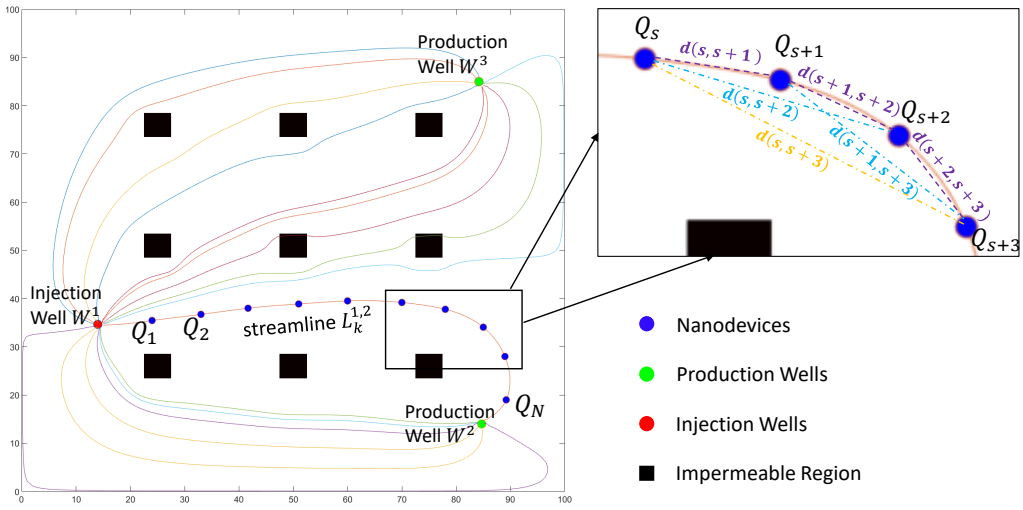

Figure 3: N nanodevices are deployed on the streamline $L_k^{1,2}$. $d(s, s+1)$, $d(s, s+2)$, $d(s, s+3)$ denote the Euclidean distance between (Q_s, Q_{s+1}), (Q_s, Q_{s+2}), and (Q_s, Q_{s+3}), respectively.

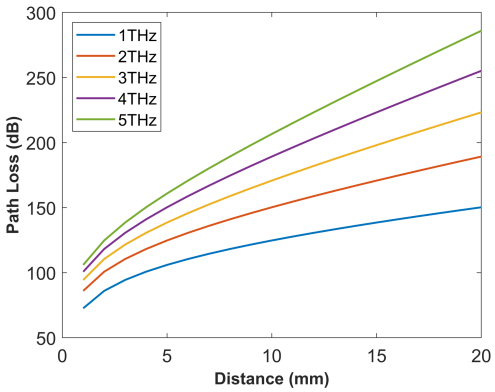

Figure 4: Path loss as a function of frequency and distance

Note when frequency f is fixed, PL only depends on d:

$$PL = PL(d). \tag{13}$$

Path loss PL obtained from Equation (13) will be used to compute receiving power P_{rv} shown in Equation (14). Note that the receiving power P_{rv} is also called the received signal strength indicator (RSSI), which is recorded in nanoreceivers. In this paper, the transmitting power P_{tx}, transmitting gain G_{tx} and receiving gain G_{rv} are assumed to be fixed for nanodevices communication while they flow along the streamlines.

$$P_{rv} = P_{tx} + G_{rv} + G_{tx} - PL \tag{14}$$

3.1.3 Communication Model. To describe how the nanodevices communicate with each other, we present the communication model here. As mentioned earlier in Section 3.1, nanosensors can only communicate with others on the same streamline. To make the notations simpler, we use $\{Q_1, Q_2, \cdots, Q_N\}$ as the points, which are locations of nanodevices, along streamline $\{L_k^{i,j}\}$ shown in Figure 3.

In the following, all Q_s will refer to a specific streamline, depending on context. We refer to the (sub-)THz EM signal communication between a pair of nanodevices Q_s and Q_t, let Q_s be the transmitter and Q_t be the receiver without loss of generality. The receivers Q_t detect RSSI sent from other nanodevices. In this paper, we assume every transmitter sends periodical THz EM signal with the same transmitting power. So, we can invert Equation (13) to compute the distance between the (nano-)transmitters and receivers.

In Figure 3, N nanodevices are deployed on the streamline $L_k^{i,j}$. Within each streamline, each nanodevice Q_s can communicate with its several predecessor and successors, such as $\{\cdots, Q_{s-2}, Q_{s-1}, Q_s, Q_{s+1}, Q_{s+2}, \cdots\}$. From Figure 4, we see the path loss increases as distance increases. So function PL defined in Equation (13) is monotonous in terms of distance d and subsequently invertible. Therefore, we define the distance function between two nanodevices Q_s and Q_t as:

$$d(s,t) := |Q_s - Q_t| = PL^{-1}(RSSI(Q_s, Q_t)) \tag{15}$$

In practice, it is hard for nanodevices to communicate when they are too far away from each other. So the distance function above is only available when |s-t| is not large. However, in this paper we only assume to know the function $d(s,t)$ when $|s-t| <= 3$, i.e. we only need the distances from six nodes $\{Q_{s-3}, Q_{s-2}, Q_{s-1}, Q_{s+1}, Q_{s+2}, Q_{s+3}\}$ to node Q_s.

3.2 Problem Formulation

In this paper, we primarily aim to map the shapes and locations of impermeable areas in an underground oil reservoir. Figure 3 gives an example of how our problem looks like. 9 square impermeable blocks are located inside a 100 ft × 100 ft reservoir. 3 wells, 1 injection and 2 production, are forming 2 well pairs. The coordinates of the 3 wells are known. The streamlines between the well pair (W^i, W^j), $1 <= i, j <= 3$, in various shapes, are bypassing the 9 impermeable blocks from different directions.

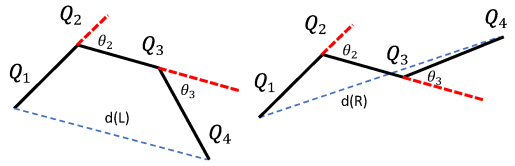

Figure 5: Two possible shapes of four-point polyline. Q_2 and Q_3 "turn" to the same directions in the left picture and to opposite directions in the right picture.

Based on the discussion above and Equation (15), by leveraging nanotechnology, we ultimately obtain distances among each group of four consecutive neighboring nanosensors. These, combined with injection and production well coordinates, are the only input information we can leverage. The problem we aim to solve in this paper is then defined to be: Given the distance information among nanodevices, how to reconstruct the streamlines and then compute the shape and location of the impermeable areas.

4 PROPOSED SOLUTION

One can notice that the streamlines can never go through the impermeable areas but can flow really "close" along the boundary of the impermeable areas. So the basic idea to characterize the impermeable areas is to use several wells surrounding the impermeable regions, then use nanodevices to run along the streamlines among the injection wells and production wells. Overlapping all the plots of streamlines collected from different pairs of wells, we can directly obtain the "inaccessible regions", which are exactly the impermeable areas from the plot. Figure 11 is the result of an example which will be explained in later sections.

The main challenge of the mapping method is how to reconstruct the shape of the streamlines since we only have the information of the distances among local sensors. Then, the next challenge is how to reconstruct the shape of all streamlines only using the distance information above. For example, if we flip a reconstructed streamline along the straight line of the injection well and the production well, the symmetric streamline still satisfies all distance criteria. Consequently, we have to pick the correct streamline among all possible solutions. We solve these two challenges as follows.

4.1 Local Reconstruction

Our claim is that knowing the Euclidean distances among four sequential points is enough to reconstruct the shape of the four-point polyline under rigid body transformation. If we know the distances from each point along the streamline to its three predecessor points and its three successor points, we can exactly reconstruct the shape of the whole streamline under rigid body transformation.

Given four points $\{Q_1, Q_2, Q_3, Q_4\}$, the only information we have is the six distances $d_{ij} = |Q_i - Q_j|, i \neq j$. So we can use d_{12}, d_{23} and d_{13} to compute the positive external angle θ_2 between vector $\overrightarrow{Q_1Q_2}$ and vector $\overrightarrow{Q_2Q_3}$ in figure 5 from:

$$\theta_i = \pi - \arccos \frac{(Q_{i-1} - Q_i) \cdot (Q_{i+1} - Q_i)}{|Q_{i-1} - Q_i||Q_{i+1} - Q_i|}. \tag{16}$$

The same way we can compute θ_3. Notice this external angle is only the absolute value of the angle, we don't know the sign, i.e. we don't know if the angle "turns" to the left or right.

Since we have now the distances d_{12}, d_{23}, d_{13} and the two external angles θ_2 and θ_3, there are only two possible shapes for the four points shown in Figure 5. Fortunately in the two shapes in figure 5, the distances between Q_1 and Q_4 are different. More specifically, we can use analytical geometry to compute the closed form of the squared distance between Q_1 and Q_4 in the left shape and right shape in Figure 5 as follows:

$$d(L)^2 = \frac{d_{12}^2 - d_{23}^2 + d_{34}^2 + d_{13}^2 + d_{24}^2}{2} + \frac{(d_{12}^2 - d_{13}^2)(d_{34}^2 - d_{24}^2)}{2d_{23}^2} - 16\frac{\Delta(Q_1, Q_2, Q_3)\Delta(Q_2, Q_3, Q_4)}{2d_{23}^2} \tag{17}$$

$$d(R)^2 = \frac{d_{12}^2 - d_{23}^2 + d_{34}^2 + d_{13}^2 + d_{24}^2}{2} + \frac{(d_{12}^2 - d_{13}^2)(d_{34}^2 - d_{24}^2)}{2d_{23}^2} + 16\frac{\Delta(Q_1, Q_2, Q_3)\Delta(Q_2, Q_3, Q_4)}{2d_{23}^2}, \tag{18}$$

where $\Delta(\cdot, \cdot, \cdot)$ is the absolute value of the area of a triangle, which is unique to the lengths of three edges of the triangle. Then we compare d_{14} to the two distances above. If d_{14} equals $d(L)$, then vertices Q_2 and Q_3 must "turn" to the same direction. If d_{14} equals $d(R)$, Q_2 and Q_3 must "turn" to opposite directions. Now we claim that the six distances can uniquely define the shape of the four-point polyline.

As for the whole streamline, we can use the local reconstruction to compute a unique curve under translation, rotation and reflection. Given vertices $\{Q_1, Q_2, \cdots, Q_N\}$, we use Equation (16) to compute positive external angles: $\{\theta_s | s = 2, 3, \cdots, N-1\}$. Then we use the condition above on vertices $\{Q_{s-1}, Q_s, Q_{s+1}, Q_{s+2}\}$ to check if θ_s and θ_{s+1} will "turn" to the same directions.

Assume vertex Q_1 is always at the original point (0,0), and Q_2 is $(d_{12}, 0)$ and θ_2 is positive, i.e., $\{Q_1, Q_2, Q_3\}$ is "turning" left. Assume we know the location of $\{Q_1, Q_2, \cdots, Q_s\}$, then we know the value and sign of θ_{s-1} and vector $Q_{s-1}Q_s$. We can compute angle θ_s, we know the distance $d_{s,s+1}$, then we can compute the location of Q_{s+1}. By mathematical induction, we can compute the locations of all $\{Q_1, Q_2, \cdots, Q_N\}$. Thus we proved we can reconstruct the shape of the whole streamline. If θ_2 has the opposite sign, i.e., Q_2 is "turning" right, then we obtain the only other curve satisfying all geometry criteria. In the next section, we'll show how to pick between the two curves.

4.2 Global Reconstruction

Using the local reconstruction, we reconstruct the shapes of all streamlines originated at (0,0). Then we rotate and translate all streamlines separately so that the start and end points of each streamline are aligned to the injection and production wells associate to the streamline. The left side of Figure 6 shows the result of the translation and rotation.

Each streamline can be flipped along the straight line through the injection and production wells. Notice that a streamline cannot intersect with other streamlines. First we compute the total number of intersections of all curves. Each time we pick one curve $L_k^{i,j}$ with most intersections and the set of curves intersecting with $L_k^{i,j}$:

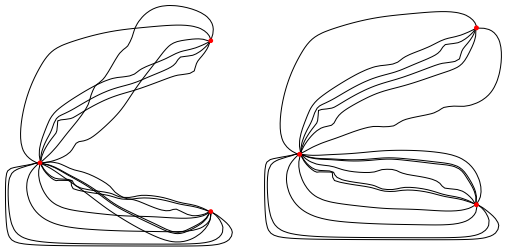

Figure 6: Left: each streamline is reconstructed separately so they may intersect with each other. Right: some of the streamlines are flipped properly, no intersection indicates we reconstructed the streamline successfully.

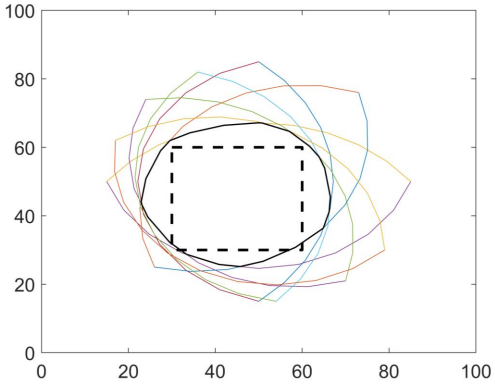

Figure 7: [1] solution: a near-circle shape outlined with solid black line is formed by arc reconstruction for approximate IR characterization. The coordinates of 4 IR vertices are (31,31), (60,31), (60,60) and (31,60).

$\widetilde{L_k^{i,j}} = \{L_t | L_t \cap L_k^{i,j} \neq \emptyset \& L_t \neq L_k^{i,j}\}$. We try to flip curve $L_k^{i,j}$ or the set $\widetilde{L_k^{i,j}}$ to see which one would lead to a larger intersection number reduction. Then flip that curve or curve set. We found in our experiments that this heuristic greedy method can find the correct answer with half the number of streamline iterations. Other picking methods could be adopted but were beyond the scope of this paper. The right side in Figure 6 shows the result of our flipping which is the final result of our reconstruction algorithm.

5 PERFORMANCE EVALUATION

In this section, we compare our streamline reconstruction solution with the state of the art [1] (SOTA) by visualizing the quality of the IR mapping. We ran our streamline reconstruction solution based on the same experiment set up as in [1]: a $100 \times 100 ft^2$ reservoir with a $30 \times 30 ft^2$ IR. For the sake of generality, we set the position of the IR at an off-center position. The square box with black dashed outline in Figure 7 denotes the IR. This experiments set up also applies to our streamline reconstruction solution.

In Figure 7, after deploying 12 mapping operations (i.e., 12 wells), the SOTA arc reconstruction solution approximately characterizes the single IR with a near-circle shape outlined with black solid lines. We can see clearly that the near-circle shape still does not match with the square IR, indicating the potential for improvement. On the contrary, when the 12 wells are deployed, we see our near 100% accurate characterization in Figure 8. All streamlines combined give the exact shape and locations of the squared IR depicted with dashed lines. This shows our streamline reconstruction outperforms the SOTA solution [1].

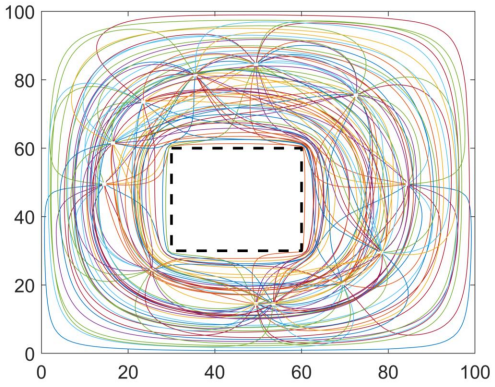

Figure 8: Proposed solution: streamline reconstruction achieves nearly 100% accuracy in IR characterization.

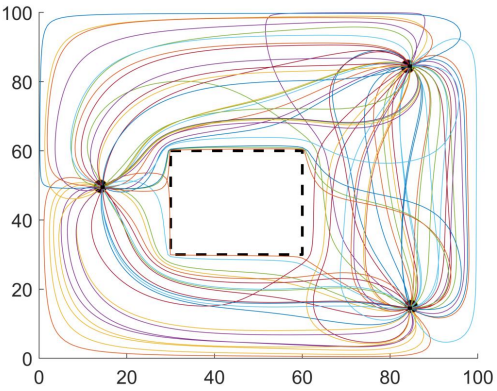

Figure 9: With 3 wells employed, a near-optimal characterization can still be achieved using streamline reconstruction

We also show an additional advantage of streamline reconstruction (i.e., proposed solution) over SOTA arc reconstruction [1]: streamline reconstruction is more efficient, with fewer resources needed. In Figure 9, where only 3 wells are deployed, we still see near optimal characterization performance, which is much better than that in Figure 7 requiring 12 wells. In light of extremely high cost of drilling wells, our solution reduces the exploration expenses to a great extent.

The proposed streamline reconstruction solution also enjoys the benefits of the high generality for highly heterogeneous reservoirs, which reflects the realism in real reservoirs. In Figure 10, 4 IRs represent higher heterogeneity in the reservoir compared the single IR in Figure 7. Figure 10 shows that SOTA solution finally reaches a near-square characterization outlined with black solid line, which does not match with any of the 4 IRs. This unveils the underlying single IR problem scenario assumption of SOTA solution, which consequently undermines the SOTA solution performance in the

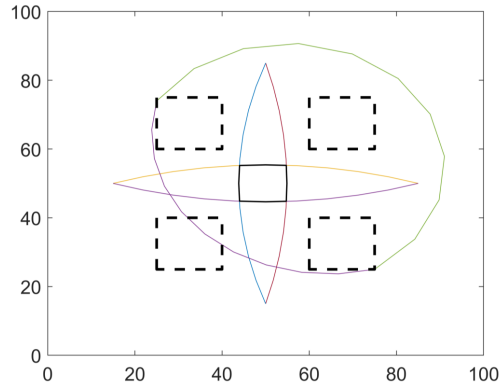

Figure 10: [1] Solution: For the reservoir with higher heterogeneity, arc reconstruction solution cannot achieve feasible mapping performance

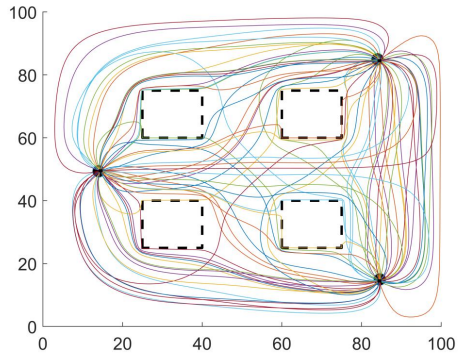

Figure 11: Proposed solution: Streamline reconstruction solution still characterizes the higher heterogeneous reservoir with near-optimal accuracy.

problem scenario with more than one IR. In contrast, we can still characterize the 4 IRs with near optimal accuracy using streamline reconstruction solution. In Figure 11, 3 wells are employed to accurately characterize the shapes and locations of all of the 4 IRs.

6 CONCLUSIONS AND FUTURE WORK

During conventional oil reservoir explorations, the existence of impermeable regions hinders the performance of current production system. Precise characterizations of those impermeable regions plays a key role in improving overall production system performance. In this paper, by exploiting nanodevices' THz communication capability, we characterize shapes and locations of IRs in highly heterogeneous oil reservoirs. We present a THz channel model for such nano-communications between nanosensors, which are initially injected into underground through injection wells. As nanosensors move through the oil reservoir, they flow along the simulated paths, i.e. streamlines, to the production wells. We present a general path reconstruction workflow to map the path shapes. In this way, we map the shapes and locations of IRs. Through comparisons with state of the art solutions, we show the superior performances of our method. Ideas for future work are as follows: a) In this paper we do not consider the RSSI measurements errors due to noise. This will result in inaccurate distances among nanosensors. For our particular application in this paper, the spatial and temporal variations of water and oil saturation in the underground reservoir may lead to additional spatial and temporal distance noises; b) The generic nanosensor path reconstruction workflow has potential for applications in many other areas, e.g., medical imaging and micro-robots localization in disaster areas.

ACKNOWLEDGMENTS

This work was supported by NSF grant #1253968. We thank Schlumberger for the Eclipse software license donation.

REFERENCES

[1] L. Jin, L. Zuo, Z. Yan, and R. Stoleru. Nanocommunication-based impermeable region mapping for oil reservoir exploration. In *ACM International Conference on Nanoscale Computing and Communication (NanoCom)*, 2019.
[2] X. Kong and M.M. Ohadi. Application of micro and nano technologies in the oil and gas industry-overview of recent progress. In *Proceedings of the SPE Abu Dhabi International Petroleum Exhibition and Conference*, 2010.
[3] H. Saadawi. Application of renewable energy in the oil and gas industry. In *Society of Petroleum Engineers*, April 2019.
[4] A. Shams A. Al-Ali, K. Stephen. Toward reservoir characterization-comparing inversion methods of a heterogeneous carbonate reservoir in supergiant onshore field. In *International Petroleum Technology Conference*, January 2020.
[5] P. S. Denis and D. T. Thierry-Laurent. Wellbore far-field imaging for high resolution reservoir characterization. In *International Petroleum Technology Conference*, January 2020.
[6] P. Britto and A. Sageev. The effects of size, and orientation of an impermeable region on transient pressure testing. In *SPE California Regional Meeting*, 1987.
[7] M. Nestor and C. Heber. Detection of linear impermeable barriers by transient pressure analysis. In *SPE Conference Paper*, Utah, USA, 1983.
[8] S. H. Zhang, Y. Xu, M. Abu-Ali, and M. K. Teng. Seismic facies recognition and stratigraphic trap characterization based on neural networks. In *International Petroleum Technology Conference*, March 2019.
[9] D. Qiu, R. Vamegh, B. Damjanac, and X. Wan. Narrow versus wide fairway fracture geometry. In *U.S. Rock Mechanics/Geomechanics Symposium*, June 2019.
[10] S. Anusarn, L. Jiawei, and W. Kan. Development of efficiently coupled fluid-flow/geomechanics model to predict stress evolution in unconventional reservoirs with complex-fracture geometry. *SPE Journal*, 2018.
[11] M. Vuran and I. F. Akyildiz. Channel model and analysis for wireless underground sensor networks in soil medium. *Physical Communication*, 3(4):245 – 254, 2010.
[12] I. F. Akyildiz, Z. Sun, and M. Vuran. Signal propagation techniques for wireless underground communication networks. *Physical Communication*, 2(3):167 – 183, 2009.
[13] A. Sangwan, H. Pandey, P. Johari, and J. M. Jornet. Increasing the communication distance between nano-biosensing implants and wearable devices. In *2018 IEEE 19th International Workshop on Signal Processing Advances in Wireless Communications (SPAWC)*, pages 1–5, 2018.
[14] M. A. Akkaş, I. F. Akyildiz, and R. Sokullu. Terahertz channel modeling of underground sensor networks in oil reservoirs. In *2012 IEEE Global Communications Conference (GLOBECOM)*, pages 543–548, 2012.
[15] M. A. Akkas. Channel modeling of wireless sensor networks in oil. *Wireless Personal Communications*, 95:4337–4355, 2017.
[16] A. Datta-Gupta and M.J. King. *Streamline Simulator*. Society of Petroleum Engineers, Richardson, Texas A&M University, 2005.
[17] L.H. Zuo, J. Lim, R.Q. Chen, and M.J. King. Efficient calculation of flux conservative streamline trajectories on complex and unstructured grids. In *78th EAGE Conference and Exhibition*, Vienna, Austria, 2016.
[18] M.R. Thiele, R.P. Batycky, and D.H. Fenwick. streamline simulation for modern reservoir-engineering workflows. *Journal of Petroleum Technology*, 62, 2010.
[19] Matthew N. O. Sadiku. *Elements Of Electromagnetics*. 3rd. edition, 1989.
[20] N. R. Peplinski, F. T. Ulaby, and M. C. Dobson. Corrections to "dielectric properties of soils in the 0.3-1.3-ghz range". *IEEE Transactions on Geoscience and Remote Sensing*, 33(6):1340–, 1995.
[21] N. R. Peplinski, F. T. Ulaby, and M. C. Dobson. Dielectric properties of soils in the 0.3-1.3-ghz range. *IEEE Transactions on Geoscience and Remote Sensing*, 33(3):803–807, 1995.
[22] T. Meissner and F. J. Wentz. The complex dielectric constant of pure and sea water from microwave satellite observations. *IEEE Transactions on Geoscience and Remote Sensing*, 42(9):1836–1849, 2004.